Applied Physics Letters

Theory of thermal radiation from a nanoparticle array

Cite as: Appl. Phys. Lett. **121**, 241701 (2022); https://doi.org/10.1063/5.0117131
Submitted: 30 July 2022 • Accepted: 05 December 2022 • Published Online: 14 December 2022

Hakan Salihoglu, Zhuo Li and Sheng Shen

AIP Publishing

Theory of thermal radiation from a nanoparticle array

Cite as: Appl. Phys. Lett. **121**, 241701 (2022); doi: 10.1063/5.0117131
Submitted: 30 July 2022 · Accepted: 5 December 2022 ·
Published Online: 14 December 2022

Hakan Salihoglu, Zhuo Li, and Sheng Shen[a)]

AFFILIATIONS

Department of Mechanical Engineering, Carnegie Mellon University, Pittsburgh, Pennsylvania 15213, USA

Note: This paper is part of the APL Special Collection on Thermal Radiation at the Nanoscale and Applications.
[a)]**Author to whom correspondence should be addressed:** sshen1@cmu.edu

ABSTRACT

Thermal radiation has diffusive and broad emission characteristics. Controlling emission spectrum and direction is essential for various applications. Nanoparticle arrays, supporting collective lattice resonances, can be employed for controlling optical properties. However, thermal emission characteristics remain unexplored due to the lack of a theoretical model. Here, we develop an analytical model to predict thermal radiation from a nanoparticle array using fluctuation–dissipation theorem and lattice Green's functions. Our findings reveal that the periodicity and particle size of the particle array are main parameters to control both emission spectrum and direction. The derived simple expression for thermal emission enables insightful interpretation of physics. This model will lay a foundation for analytical derivation of thermal radiation from metasurfaces. Our study can be useful in engineering infrared thermal sources and radiative cooling applications.

Controlling and tuning thermal emission spectrum is essential for a variety of applications, such as energy conversion and waste heat recovery,[1,2] sensing,[3] microscopy,[4] and illumination.[5] Conventional materials used in these applications are bulky, and their intrinsic radiative properties are insufficient for multiple functionalities.[6] Metasurfaces, on the other hand, are compact, ultrathin, and relatively easy to fabricate and have emerged as a promising platform for tailoring thermal radiative properties.[3,7–11] Arrangement of "meta-atoms," configurability of array structures, and shape of the elements in the metasurfaces enable high degrees of freedom to control and tune the emission spectrum. However, the prediction of these properties mainly relies on exhaustive and repetitive computational methods. Identifying important parameters in the design of thermal metasurfaces requires a comprehensive analytical model.

Narrow-band and highly directional emission requires spatial and temporal coherence in thermal emitters.[12,13] Several techniques, such as photonic crystals,[14,15] grating structures,[12] nanostructured surfaces,[7] and nanoantennas,[16,17] have been employed to achieve coherence. Another possible technique can be realized by exploiting lattice resonances. Excitation of conduction-electrons within metallic nanostructures induces localized surface-plasmon resonances. Arranged in an array form, these nanoresonators can respond to excitations collectively and induce temporal and spatial coherence. These collective responses give rise to collective lattice resonances (CLRs) when the array periodicity is comparable to the wavelength.[18–23] Theoretical modeling of CLR relies on dipole approximations, and the CLRs can be accounted by lattice sums under the approximation. Extensively analyzed in the photonics field,[24–26] CLRs have not been discussed in the field of thermal radiation yet. Also, even though multiple studies[27–30] have investigated lattice structures in thermal radiation, CLRs have never been investigated.

In this Letter, we derive an analytical model to predict thermal radiation from a nanoparticle array with a unit cell consisting of a single emitter using coupled dipole approximation. Our aim is to show the capability of CLRs to tune and control thermal emission spectrum and directionality. To express thermal radiation, we exploit the correlation of fluctuating dipoles in a given environment using fluctuation–dissipation theorem. Then, by means of lattice summations, also known as Ewald's sum, we can finalize the derivation of our theory. Consequently, we examine the role of periodicity and size of nanostructures in controlling spectral and directional thermal emission. The derived model will also provide a basis for extension to understand the thermal emission from metasurfaces. Here, we choose to work with the simplest situation, in which the nanoparticle is described by its polarizability, so that an emitter particle in the array couples to neighboring particles through dipole–dipole interaction only.

To derive the model, we consider a periodic array of nanostructures. The array consists of single-structure unit cells extending in free-space with the periodicities of a and b along the x- and y-axis, i.e., rectangular lattice, respectively. Nanostructures in the array are held at temperature T_p and embedded in an environment at T_{env}. The array and the environment form a global system. Figure 1 shows the schematic of the system under consideration.

To derive the emitted heat by the array, we need to find the Poynting vector, proportional to $\langle \boldsymbol{E} \otimes \boldsymbol{H}^* \rangle$, where E and H stand for the electric and magnetic fields, respectively, $\langle \dots \rangle$ represents the ensemble average, $\otimes$ is the tensor product, and $*$ is the complex conjugate. Using the additivity property of the electric field, we define the total electric field $\boldsymbol{E}(\boldsymbol{r}, \omega)$ at position $\mathbf{r}$ in the frequency domain (ω-angular frequency) as

$$\boldsymbol{E}^{tot}(\boldsymbol{r}, \omega) = \boldsymbol{E}^{bath}(\boldsymbol{r}, \omega) + \boldsymbol{E}^{ind}(\boldsymbol{r}, \omega). \tag{1}$$

Here, $\boldsymbol{E}^{bath}$ is the background field of thermal radiation from a thermal bath. $\boldsymbol{E}^{ind}$ denotes the electric field induced by the nanostructures in the array. Given that the dimension of nanostructures is comparably small with respect to wavelength, the optical response of the nanostructure at position $\boldsymbol{r_i}$ can be modeled as a point dipole with a dipole moment $\boldsymbol{p}_i$. Using the dipole approximation, $\boldsymbol{E}^{ind}$ is expressed as the summation of the fields generated by the dipoles,

$$\boldsymbol{E}^{ind} = \omega^2 \mu_o \sum_i \mathbb{G}_E^{(o)}(\boldsymbol{r}, \boldsymbol{r}_i) \boldsymbol{p}_i, \tag{2}$$

where i stands for the ith particle in the array and $\mathbb{G}_E^{(o)}$ represents the dyadic Green's function in free-space relating the source (dipole moment) with the electric field at $\boldsymbol{r} (= \boldsymbol{R}, z)$.[31] Contribution to the dipole moment of the ith particle arises from fluctuating and induced parts,[32]

$$\boldsymbol{p}_i = \boldsymbol{p}_i^{fl} + \boldsymbol{p}_i^{ind} = \boldsymbol{p}_i^{fl} + \varepsilon_0 \alpha_i \left(\boldsymbol{E}_i^{bath} + \omega^2 \mu_o \sum_{j \neq i} \mathbb{G}_E^{(o)}(\boldsymbol{R}_i, \boldsymbol{R}_j) \boldsymbol{p}_j \right), \tag{3}$$

where ε_0 is the vacuum permittivity and α_i is the dynamic polarizability of the dipole. Dipole moment, $\boldsymbol{p}_i$, can be defined in terms of the exciting and external fields of the thermal bath, $\boldsymbol{E}_i^{bath}$, and its fluctuating dipole moment, $\boldsymbol{p}_i^{fl}$. Consequently, effective polarizability, α_e, of a dipole, defined as the optical response of a unit cell to an external field in a given environment, can be found by following the derivation given in Ref. 23. Hence, $\boldsymbol{p}_i$ is cast into the following form:

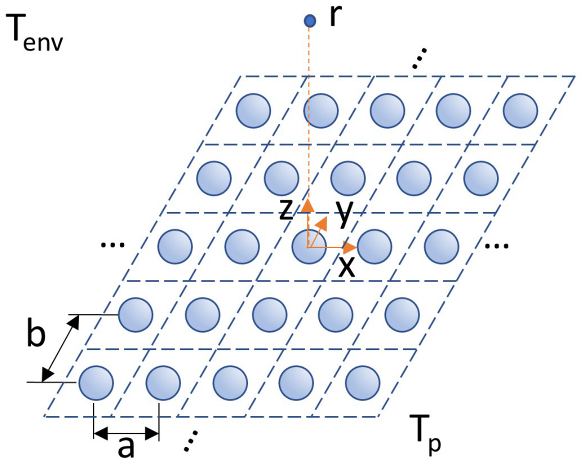

FIG. 1. General schematic of a 2D infinite array with emitting nanoparticles.

$$\boldsymbol{p}_i = \mathbb{A} \boldsymbol{p}_i^{fl} + \varepsilon_0 \overset{\leftrightarrow}{\alpha}_e \boldsymbol{E}_i^{bath}, \tag{4}$$

where $\mathbb{A} = \left(\mathbb{I} - k_o^2 \alpha_i \mathbb{G}_E^{(l),\neq}(\boldsymbol{k}_\parallel) \right)^{-1}$ with wavenumber, k_o, in free-space and effective polarizability matrix, $\overset{\leftrightarrow}{\alpha}_e = (\alpha_i^{-1} \mathbb{I} - k_o^2 \mathbb{G}_E^{(l),\neq}(\boldsymbol{k}_\parallel))^{-1}$. We note that effective polarizability is a function of the in-plane component of wavevector, $k_\parallel$. This parameter is the main contribution to the existing dipole based radiation models in Refs. 33–36 and contains the condition that gives rise to CLRs. In this study, we consider tungsten sphere nanoparticles and the dynamic polarizability of the sphere reads[37] $\alpha_i = (\alpha_o^{-1} - i k_o^3 / 6\pi)^{-1}$, where α_o is the bare polarizability equal to $4\pi (d/2)^3 (\epsilon - 1)/(\epsilon + 2)$ and ϵ and d are the dielectric function and the diameter of the sphere, respectively. The dielectric functions for tungsten are taken from Ref. 38. Here, $\mathbb{G}_E^{(l),\neq}(\boldsymbol{k}_\parallel)$ is the so-called lattice sum and given as $\sum_{j \neq i} \mathbb{G}_E^{(o)}(\boldsymbol{R}_i, \boldsymbol{R}_j) e^{i \boldsymbol{k}_\parallel \cdot (\boldsymbol{R}_i - \boldsymbol{R}_j)}$. The sum excludes emission by the dipole i because its self-interaction is considered in dynamic polarizability by radiative damping,[25] and the exclusion is indicated by superscript $\neq$. In our study, numerical calculation of lattice sum for the effective polarizability relies on Ewald's sum.[39,40] To minimize the loss of accuracy in numerical computations at high frequencies (radiation wavelength is smaller than periodicity), we have taken a special care by following the suggestions given in Refs. 41 and 42.

To obtain the total electric field at $\boldsymbol{r}$, Eq. (4) is inserted into Eq. (2), and the resultant expression is substituted into Eq. (1). Then, we obtain

$$\boldsymbol{E}^{tot}(\boldsymbol{r}, \omega) = \boldsymbol{E}^{bath}(\boldsymbol{r}, \omega) + \mu_o \omega^2 \left(\mathbb{G}_E^{(l)}(\boldsymbol{k}_\parallel) \mathbb{A} \boldsymbol{p}_o^{fl} + \mathbb{G}_E^{(l)}(\boldsymbol{k}_\parallel) \overset{\leftrightarrow}{\alpha}_e \boldsymbol{E}_o^{bath} \right). \tag{5}$$

Here, $\mathbb{G}_E^{(l)}(\boldsymbol{k}) = \sum_i \mathbb{G}_E^{(o)}(\boldsymbol{r}, \boldsymbol{r}_i) \boldsymbol{e}^{i \boldsymbol{k}_\parallel \cdot \boldsymbol{R}_i}$ runs over all the dipoles in the array. Subscript o stands for the dipole located at $\boldsymbol{r}_o = (0, 0, 0)$. With the same procedure, $\boldsymbol{H}^{tot}(\boldsymbol{r}, \omega)$ in the Poynting vector expression can be derived. Here, we note that the lattice Green's function is a result of summation over all the dipoles in the array and expressed with far-field approximation. Expressions for the lattice sum in the far-field can be found in Ref. 39.

After deriving electric and magnetic fields at position $\boldsymbol{r}$ [$= (0, 0, z)$] for a given $k_\parallel$, the Poynting vector can be evaluated. Using the symmetry about the x- and y-axis, we can express the Poynting vector across a plane at an arbitrary distance z from the array plane as $P_{\omega, k_\parallel}^{tot} = 2 Re \epsilon_{ijz} \langle \boldsymbol{E}^{tot} \otimes \boldsymbol{H}^{tot,*} \rangle_{ij}$. To find the correlation function, we take the tensor product of Eq. (5) and the complex conjugate of magnetic field, $\boldsymbol{H}^{tot,*}$, and eliminate uncorrelated interactions, $\langle \boldsymbol{E}^{bath} \otimes \boldsymbol{p}_o \rangle$.[43] $P_{\omega, k_\parallel}^{tot}$ can be expressed as a summation of $P_{\omega, k_\parallel}^{array}$ and $P_{\omega, k_\parallel}^{bath}$, where

$$P_{\omega, k_\parallel}^{array} = 2 Re \epsilon_{ijz} \left\{ \omega^4 \mu_o^2 \mathbb{G}_E^{(l)} \mathbb{A} \left\langle \boldsymbol{p}_o^{fl} \otimes \boldsymbol{p}_o^{fl,*} \right\rangle \mathbb{A}^* \mathbb{G}_H^{(l),*} \right\}_{ij}, \tag{6}$$

$$\begin{aligned} P_{\omega, k_\parallel}^{bath} = 2 Re \epsilon_{ijz} \Big\{ & \left\langle \boldsymbol{E}^{bath} \otimes \boldsymbol{H}^{bath,*} \right\rangle + \omega^2 \mu_o \left\langle \boldsymbol{E}^{bath} \otimes \boldsymbol{E}_o^{bath,*} \right\rangle \overset{\leftrightarrow}{\alpha}_e^* \mathbb{G}_H^{(l),*} \\ & + \omega^2 \mu_o \mathbb{G}_E^{(l)} \overset{\leftrightarrow}{\alpha}_e \left\langle \boldsymbol{E}_o^{bath} \otimes \boldsymbol{H}^{bath,*} \right\rangle \\ & + \omega^4 \mu_o^2 \mathbb{G}_E^{(l)} \overset{\leftrightarrow}{\alpha}_e \left\langle \boldsymbol{E}_o^{bath} \otimes \boldsymbol{E}_o^{bath,*} \right\rangle \overset{\leftrightarrow}{\alpha}_e^* \mathbb{G}_H^{(l),*} \Big\}_{ij}. \end{aligned} \tag{7}$$

Here, ϵ_{ijz} is the Levi–Civita tensor. As $P^{array}_{\omega,k_\parallel}$ accounts for thermal emission from the array, $P^{bath}_{\omega,k_\parallel}$ indicates the background contribution.

The correlation of background fields as well as fluctuating dipoles depends on equilibrium conditions. Under global equilibrium, i.e., $T_p = T_{env}$, the correlation of background fields in Eq. (7) reads[44] $\langle \boldsymbol{E}^{bath} \otimes \boldsymbol{H}^{bath,*}\rangle = -2i\Theta_p\mu_o\omega Re(\mathbb{G}^{(o)}_H)$ and $\langle \boldsymbol{E}^{bath} \otimes \boldsymbol{E}^{bath,*}\rangle = 2\Theta_{env}\mu_o\omega Im(\mathbb{G}^{(o)}_E)$, where $\Theta_i = \hbar\omega/\left(e^{(\hbar\omega)/(k_B T_i)} - 1\right)$ is the mean energy of a harmonic oscillator in thermal equilibrium at temperature T_i. The correlation of the dipole fluctuations in the presence of an environment is given by fluctuation–dissipation theorem using the effective polarizabilities,[45,46]

$$\left\langle \boldsymbol{p}^{fl}_o \otimes \boldsymbol{p}^{fl,*}_o \right\rangle = \frac{2\Theta_b}{\mu_o\omega^3}\mathbb{A}^{-1}\left(k_o^2\frac{\overleftrightarrow{\alpha}_e - \overleftrightarrow{\alpha}^*_e}{2i} - k_o^4\overleftrightarrow{\alpha}_e\frac{\mathbb{G}^{(l)}_E - \mathbb{G}^{(l),*}_E}{2i}\overleftrightarrow{\alpha}^*_e\right)\mathbb{A}^{*-1}. \tag{8}$$

At local equilibrium, i.e., $T_p \neq T_{env}$, the background correlations are still at thermal equilibrium with temperature T_{env}. For the fluctuating dipole correlations, Eq. (8) is used with Θ evaluated at T_p.

Rearranging lattice Green's functions in Eq. (7) after inserting the background correlations and comparing the final form with $P^{array}_{\omega,k_\parallel}$, we find that $P^{array}_{\omega,k_\parallel} = -P^{bath}_{\omega,k_\parallel}$ at global equilibrium. That is, the net heat exchange between the dipole array and the background is zero; hence, $P^{tot}_{\omega,k_\parallel} = 0$. We also note that the final form of $P^{bath}_{\omega,k_\parallel}$ and $P^{array}_{\omega,k_\parallel}$ is similar to Eqs. (29) and (38) in Ref. 46, respectively. Our derivation neglects magnetic dipole contribution. Also, the effective polarizability derived in this study is implemented to fluctuation–dissipation theorem. Finally, we omit integration over the surface of a detector. $P^{tot}_{\omega,k_\parallel} = 0$ under equilibrium shows that the detailed balance is satisfied in the system at global equilibrium. Thus, our findings allow us to generalize the heat flux from the dipole array at any T_p as

$$P^{tot}_{\omega,k_\parallel} = 4\left[\Theta_p - \Theta_{env}\right]\omega\mu_o Re \times\left\{\mathbb{G}^{(l)}_E\left(k_o^2\frac{\overleftrightarrow{\alpha}_e - \overleftrightarrow{\alpha}^*_e}{2i} - k_o^4\overleftrightarrow{\alpha}_e\frac{\mathbb{G}^{(l)}_E - \mathbb{G}^{(l),*}_E}{2i}\overleftrightarrow{\alpha}^*_e\right)\mathbb{G}^{(l),*}_H\right\}. \tag{9}$$

Equation (9) gives the heat flux from an array structure at temperature T_p in a thermal bath with temperature T_{env}. We recognize that Eq. (9) resembles Eq. (80) in Ref. 36 and Eq. (15) in Ref. 34. The difference arises from the neglected background and, in turn, the absence of effective polarizability. Using far-field lattice Green's functions, $\mathbb{G}^{(l)}_E$ and $\mathbb{G}^{(l),*}_H$, explicitly given in Ref. 39, we further simplify directional and spectral thermal emission as

$$\begin{aligned} P^{tot}_{\omega,k_\parallel} = {} & 4\left[\Theta_p - \Theta_{env}\right]\frac{4\pi^2}{A^2}\sum_{\overline{m}\overline{n},|\boldsymbol{k}_{\overline{m}\overline{n}}|\le k_o}\frac{1}{k_{z,\overline{m}\overline{n}}} \\ & \times\Bigg[(1-\mathcal{E}_x\mathcal{E}_x)\left\{k_o^2 Im\left(\overleftrightarrow{\alpha}_{e,xx}\right) - k_o^4\overleftrightarrow{\alpha}_{e,xx}Im\left(\mathbb{G}^{(o)}_{E,xx} + \mathbb{G}^{(l),\neq}_{E,xx}\right)\overleftrightarrow{\alpha}^*_{e,xx}\right\} \\ & +(1-\mathcal{E}_y\mathcal{E}_y)\left\{k_o^2 Im\left(\overleftrightarrow{\alpha}_{e,yy}\right) - k_o^4\overleftrightarrow{\alpha}_{e,yy}Im\left(\mathbb{G}^{(o)}_{E,yy} + \mathbb{G}^{(l),\neq}_{E,yy}\right)\overleftrightarrow{\alpha}^*_{e,yy}\right\} \\ & +\left(\mathcal{E}_y^2 + \mathcal{E}_x^2\right)\left\{k_o^2 Im\left(\overleftrightarrow{\alpha}_{e,zz}\right) - k_o^4\overleftrightarrow{\alpha}_{e,zz}Im\left(\mathbb{G}^{(o)}_{E,zz} + \mathbb{G}^{(l),\neq}_{E,zz}\right)\overleftrightarrow{\alpha}^*_{e,zz}\right\}\Bigg]. \end{aligned} \tag{10}$$

Here, $\overline{m}$ and $\overline{n}$ are the diffraction orders and $\boldsymbol{\mathcal{E}} = (\boldsymbol{r} - \boldsymbol{R}_{\overline{m}\overline{n}})/|\boldsymbol{r} - \boldsymbol{R}_{\overline{m}\overline{n}}|$. $\boldsymbol{k}_{\overline{m}\overline{n}} = \left(\boldsymbol{k}_{||,\overline{m}\overline{n}}, k_{z,\overline{m}\overline{n}}\right)$ is the wavevector of the diffracted waves where $\boldsymbol{k}_{||,\overline{m}\overline{n}} = \boldsymbol{k}_{||} + \boldsymbol{g}_{\overline{m}\overline{n}}$ and $k_{z,\overline{m}\overline{n}} = \sqrt{k_o^2 - \left|\boldsymbol{k}_{||,\overline{m}\overline{n}}\right|^2}$. $\boldsymbol{g}_{\overline{m}\overline{n}} = \overline{m}a\boldsymbol{x} + \overline{n}b\boldsymbol{y}$ is the reciprocal lattice basis vectors where $\boldsymbol{x}$ and $\boldsymbol{y}$ are the unit vectors along the x- and y-axis, respectively. A represents the area of unit cell. Our model using Bloch's theorem can be tested with the method developed in Refs. 35 and 36.

We first examine the dispersion of effective polarizability in a square lattice. Figure 2(a) shows the imaginary component of effective polarizability normalized to the particle volume, $Im(\alpha_e)/V$, with respect to in-plane momentum $k_\parallel$ and frequency. At high frequencies, free-space wavelength, λ, is smaller than periodicity ($a = 10\,\mu$m). Diffraction of radiation from neighboring particles folds the dispersion of radiation in free-space into the light cone. Thus, we observe diffraction branches. Around frequencies where $\lambda \sim$ a, the diffraction branches are connected with the hybrid bands. These bands are manifestation of CLRs and arise from the degeneracy of the first order diffraction modes in the lattice. Since we plot the dispersion as a function of in-plane momentum along x-axis, two of the first order modes are degenerate due to diffraction along y-axis, except at $k_\parallel = 0$ where four of those are degenerate. These resonances are originated from lattice configuration encoded in the lattice Green's function and lead to high extinction, $Im(\alpha_e)$. Next, we analyze tuning parameters, periodicity in lattice Green's function, and particle size in polarizability.

Resonant response of the array structure depends on the particle size. Figure 2(b) illustrates the real component of effective polarizability normalized to volume, $Re(\alpha_e)/V$, as a function of frequency for the normal excitation direction, $k_\parallel = 0$, corresponding to the condition shown by the black dashed line in Fig. 2(a). Figure 2(b) shows that at particular frequencies, the array polarizability exhibits resonance behaviors, i.e., sharp change in response around the resonance frequency, ω_{res}, and the resonance frequency shifts toward lower frequencies by increasing the particle size. The reason for the shifted frequency is that the resonance condition, $\alpha_i \sim 1/\mathbb{G}^{(l),\neq}_E$ in α_e, is met

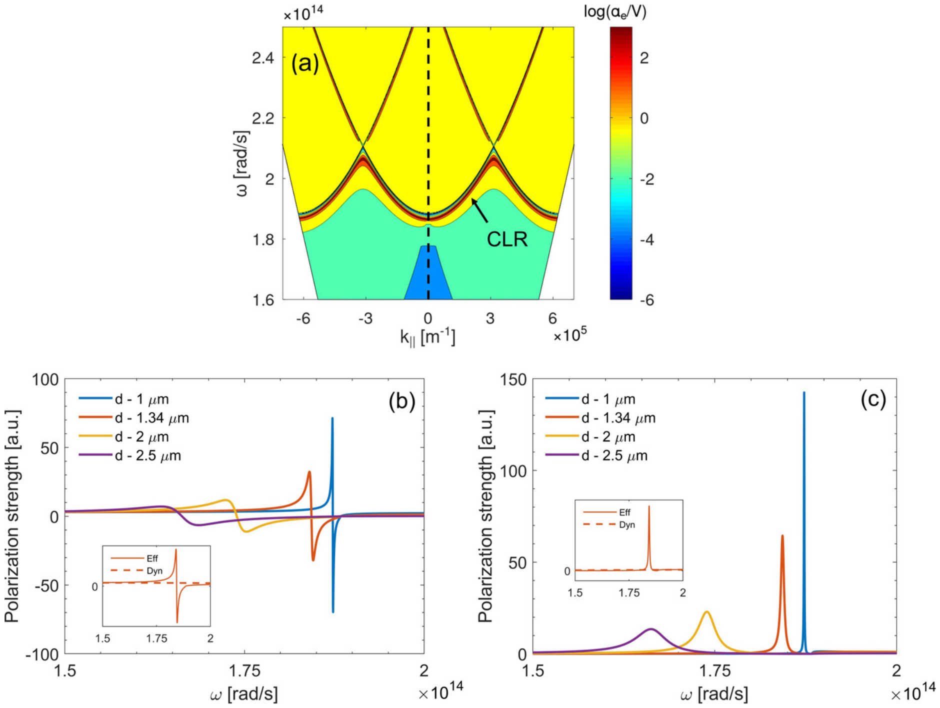

FIG. 2. (a) Band structure of CLR in an array with 10-μm periodicity and spheres of 1-μm diameter with respect to in-plane momentum $k_{\|}$. The direction of $k_{\|}$ is along the x-axis of the lattice. CLRs in the first bands are observed. Also, periodic array folds the dispersion of light cone in the frequency range where excited thermal waves have a wavelength smaller than the periodicity. (b) Real component of effective polarizability normalized to volume (α_e/V) for square lattice of particles with d= 1, 1.34, 2, and 2.5 μm and of periodicity with 10-μm when $k_{\|} = 0$. (c) Imaginary component of α_e/V in the same array given in (b). Insets in (b) and (c) show the difference between real and imaginary components of normalized dynamic and effective polarizabilities for a lattice with a particle of 1.34-μm diameter, respectively. Outside the resonance frequency, collective response of the array (related to effective polarizability) becomes same with that of an isolated particle (related to dynamic polarizability).

at lower frequencies for arrays with larger particle sizes. On the other hand, the strength of the resonant response diminishes with larger particle sizes. Figure 2(c) shows $Im(\alpha_e)/V$. In addition to diminishing resonant response, we observe broadening resonance peaks with larger sizes in both Figs. 2(b) and 2(c). The main reason for the diminishing and broadening response is that the loss related to imaginary component of dynamic polarizability, $Im(\alpha_i)$, increases for larger particles, leading to broadening and decreasing collective response.

Next, we compute spectral emission from an array with a periodicity of 10 μm at $T_p = 300$ K and $T_{env} = 0$ K using Eq. (10) and plot it in Fig. 3(a) as a function of frequency. We observe quasi monochromatic emission peaks. Comparison of Fig. 2(b) with Fig. 3(a) indicates that resonance peaks in effective polarizability coincide with the emission peaks, meaning that CLRs drive the thermal emission. Figure 3(a) also shows that arrays with larger particle sizes emit less thermal radiation. Smaller particles sustain smaller radiative damping, leading to higher quality resonance features (stronger and narrower resonance peak). In contrast, larger particles have higher radiative losses and reduce resonance quality, leading to lower and broader emission peak. To understand the role of periodicity at the emission peak frequency, we plot the spectral emission in the inset of Fig. 3(a) with respect to ratio of free-space wavelength to periodicity, λ/a. For the smallest particle size, free-space wavelength of the peak thermal emission equals the periodicity of the array, and the ratio increases with the increasing particle size. Clearly, particle size is an important parameter to tune the peak emission wavelength.

The periodicity of the array determines frequency (or wavelength) of a thermal emission peak. Figure 3(b) shows spectral thermal emission with respect to frequency for an array with periodicities of 10, 9, 8, and 7 μm. As periodicity decreases, the thermal emission peak shifts to higher frequencies. The peak frequencies, $\sim\omega_{res}$, correspond to free-space wavelength, λ, equal to the array periodicity, a. Physically, diffraction modes degenerate at wavelengths equal to the array periodicity. Based on the dispersion of free-space radiation, $\omega = 2\pi c/\lambda$, we can engineer the emission spectrum by matching $\omega_{res} \sim 2\pi c/\text{a}$. To better illustrate this phenomenon, we plot the spectral emission with respect to λ/a in the inset of Fig. 3(b). Even with smaller periodicity, the thermal emission peak happens at the free-space wavelength close to periodicity. The slight shift in the ratio from a value of 1 depends on $\mathbb{G}_E^{(l),\neq}$ in effective polarizability.

Thus far, we have analyzed spectral thermal emission for normal excitation mode, $k_{\|} = 0$. We observe that thermal radiation excites all the available modes. For better understanding of thermal emission from the nanoparticle array, we investigate directional thermal emission with respect to polar angle, θ, around the axis, z, normal to the array plane in Fig. 3(c) and with respect to azimuthal angle, $\varnothing = k_{\|}/k_o$, from the normal axis, z-axis, in the inset of Fig. 3(c). To plot Fig. 3(c) and the inset, we compute $P^{tot}_{\omega,\theta} = \int_0^{k_o/4} \frac{k_{\|}dk_{\|}}{2\pi} P^{tot}_{\omega,k_{\|}}$ and $P^{tot}_{\omega,\varnothing} = 8k_{\|}\int_0^{\pi/4} \frac{d\theta}{2\pi} P^{tot}_{\omega,k_{\|}}$, respectively, at a frequency of 1.86×10^{14} rad s^{-1} for an array of particles with d = 1.11 μm and a = 10 μm. Figure 3(c) shows that the majority of the heat at the given frequency is radiated within 10°, meaning that the heat transfer is directed to the x-axis. Due to the symmetry, we also observe the same peak near ~90° (y-axis). To plot the inset of Fig. 3(c), we assume a detector of an optical system collecting the thermal radiation with an acceptance angle of ~25° ($k_{\|}/k_o = 1/4$, receiving angle of a typical FTIR system). The inset of Fig. 3(c) peaks near normal angle ($\varnothing \sim 0$). We also plot spectral heat flux within the corresponding angle in Fig. 3(d). Spectral heat flux exhibits a peak in thermal radiation around the CLR frequency of 1.8×10^{14} rad s^{-1} [corresponding to

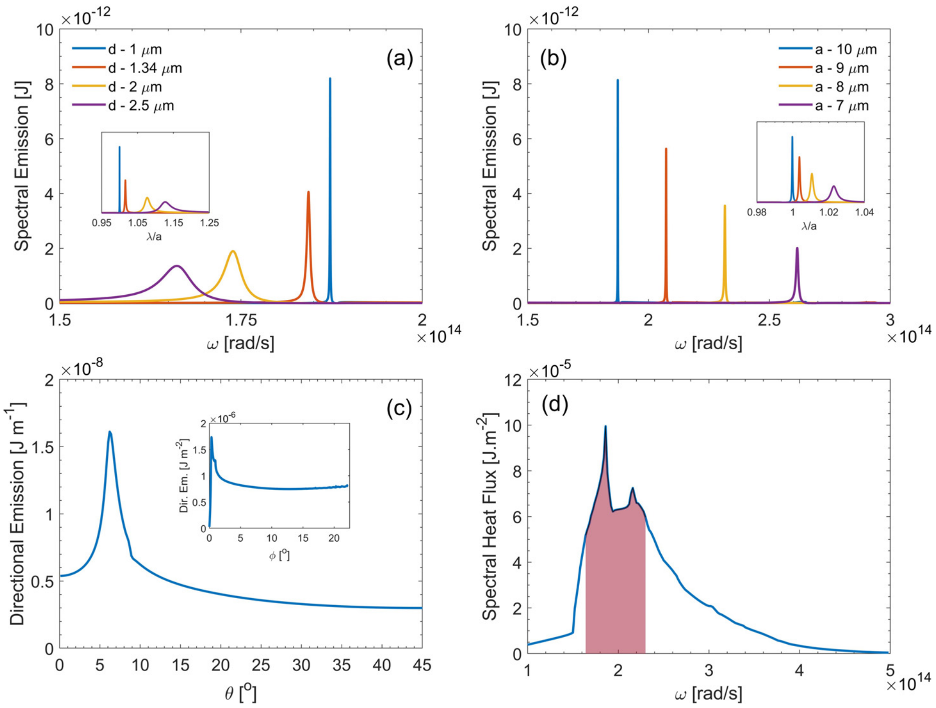

FIG. 3. Role of particle size and periodicity in thermal emission spectra. Emission profile from an array with 10-μm periodicity and various particle sizes, d, for $k_{\|} = 0$ with respect to frequency in (a) and ratio of free-space wavelength to periodicity in the inset of (a). With increasing particle size, emission peak shifts to smaller frequencies and broadens. Emission profile from arrays with periodicities of 10, 9, 8, and 7 μm for $k_{\|} = 0$ with respect to frequency in (b) and ratio, λ/a, in the inset of (b). Packing the particles more densely shifts the emission spectrum to higher frequencies and decreases the emission strength. Emission peak happens at a wavelength about the same with the periodicity ($\lambda \sim$ a). (c) Angular dependence of thermal emission with respect to polar angle, θ, around the axis normal to array plane (z-axis). (d) Spectral heat flux within an azimuthal angle of $\sim$25° over the entire polar angle range. Shaded region represents the spectral heat flux calculated to compare with the total heat flux.

a frequency between the orange and blue lines in Fig. 3(a)]. We also compute the total heat flux over the entire thermally active frequency range (not shown here) and compare the total heat flux with the spectral heat flux concentrated over a frequency range of 1.64 to 2.3×10^{14} rad s^{-1} ($\Delta\lambda \sim 3\,\mu$m, shaded region). Our comparison reveals that the spectral heat flux within the respective frequency range corresponds to >50% of the total heat flux within the considered angle.

To better understand the physical insights of CLRs, spectral thermal emission is computed using Eq. (10) and plotted as a function of in-plane momentum and frequency in Fig. 4(a), also related to dispersion relation of CLRs.[47] We find that the frequency of the orange band, the strongest thermal emission, coincides with CLR frequencies, indicating that CLRs govern major thermal emission from the array. In addition, strong CLR existence over entire in-plane momentum indicates that thermal emission direction, related to in-plane, $k_{\|}$, and free-space, k_o, momentum, can be tailored by means of CLRs. Furthermore, we observe weaker thermal emission due to diffraction modes represented by thin regions outside CLR band. For validation, we performed dispersion relation simulation in Ansys Lumerical Finite-difference Time-domain (FDTD) Solutions, and the result is shown in Fig. 4(b). From comparison of Figs. 4(a) and 4(b), we conclude that theoretical framework developed in this study approximates emission characteristics well.

In our study, we focus only on emission from an array structure under symmetric conditions. The presence of a substrate induces asymmetry in the optical environment. Experimental studies[18,20,48] demonstrate that with high contrast in refractive index of the substrate and superstrate, resonance peaks due to CLRs mainly preserve their strong and narrow profile. We notice that substrates in the mentioned studies are optically inactive in the excitation frequency range.

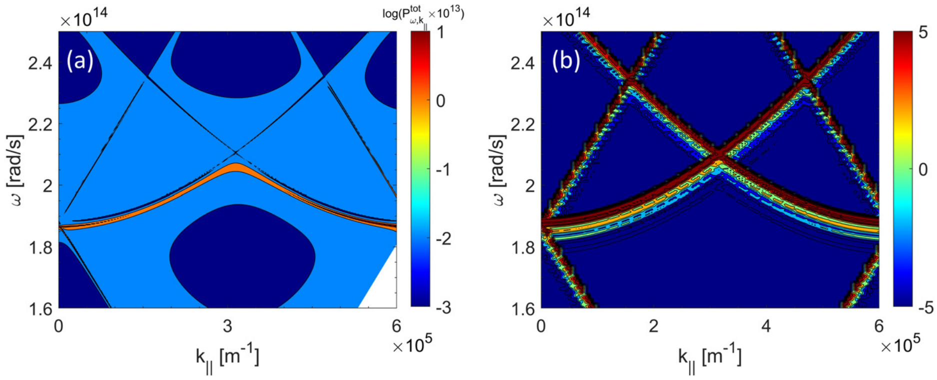

FIG. 4. The dispersion relation of an array with 10-μm periodicity and 1.11-μm particles calculated by (a) the theoretical model, and (b) FDTD simulations. The color map in (a) shows the Poynting vector [Eq. (10)] of the array; the color scale in (b) represents the averaged electrical field intensity. Both the color bars are in log scale.

Utilizing an optically active substrate, i.e., glass supporting surface phonon polaritons in the mid-infrared range, requires further consideration. These surface confined polaritons may strongly interact with coupled lattice resonances, possibly resulting in a shift in the emission frequency. On the other hand, we expect that the array structures discussed in our study will enable outcoupling of the surface confined modes to the far-field. For this type of analysis, our model needs to be extended to include the presence of a substrate. To take into account the presence of a substrate, the Green tensor or propagator in vacuum should be replaced in all our expressions by the Green tensor which takes into account the reflection with the substrate interface.

Although the array structures have finite physical sizes, the modern fabrication techniques enable fabrication of arrays as large as 1-cm^2, corresponding to 10^{10} nanostructures in a square array with a 10-μm periodicity. The optical responses of arrays in these sizes can be well approximated by those of infinite arrays, according to theoretical[49,50] and experimental[51] studies. Therefore, the assumption of infinite array structure is valid for the estimation of spectral response for many applications engineered using CLRs.

We derive an analytical model to express thermal radiation from a nanoparticle array with a single element in each unit cell. With our derivation, important lattice parameters, i.e., periodicity, particle size, and material of the particles, are implemented to the thermal radiation model. We find that CLRs observed in nanoparticle array structures enable quasi monochromatic thermal emission from an enlarged surface. The particle size and periodicity are two key parameters to tune the spectrum of thermal emission. Also, we demonstrate that CLRs represent a valuable means to control thermal emission direction at a desired frequency. We expect that this study can be expanded for metasurfaces by considering the array structure on a substrate. Also, CLRs can be useful in engineering infrared thermal sources and radiative cooling applications.

This work was supported by the Defense Threat Reduction Agency (Grant No. HDTRA1-19-1-0028) and the National Science Foundation (Grant No. CBET-1931964).

AUTHOR DECLARATIONS

Conflict of Interest

The authors have no conflicts to disclose.

Author Contributions

Hakan Salihoglu: Conceptualization (lead); Data curation (lead); Methodology (lead); Writing – original draft (lead). **Zhuo Li:** Validation (equal); Writing – review & editing (equal). **Sheng Shen:** Supervision (lead).

DATA AVAILABILITY

The data that support the findings of this study are available from the corresponding author upon reasonable request.

REFERENCES

[1] A. Lenert, D. M. Bierman, Y. Nam, W. R. Chan, I. Celanović, M. Soljačić, and E. N. Wang, Nat. Nanotechnol. **9**, 126 (2014).
[2] A. Fiorino, L. Zhu, D. Thompson, R. Mittapally, P. Reddy, and E. Meyhofer, Nat. Nanotechnol. **13**, 806 (2018).
[3] D. Costantini, A. Lefebvre, A.-L. Coutrot, I. Moldovan-Doyen, J.-P. Hugonin, S. Boutami, F. Marquier, H. Benisty, and J.-J. Greffet, Phys. Rev. Appl. **4**, 014023 (2015).
[4] P. Zijlstra, P. M. R. Paulo, and M. Orrit, Nat. Nanotechnol. **7**, 379 (2012).
[5] O. Ilic, P. Bermel, G. Chen, J. D. Joannopoulos, I. Celanovic, and M. Soljačić, Nat. Nanotechnol. **11**, 320 (2016).
[6] A. C. Overvig, S. A. Mann, and A. Alù, Phys. Rev. X **11**, 021050 (2021).
[7] H. Chalabi and A. Al, Phys. Rev. B **94**, 094307 (2016).
[8] W. Li, U. Guler, N. Kinsey, G. V. Naik, A. Boltasseva, J. Guan, V. M. Shalaev, and A. V. Kildishev, Adv. Mater. **26**, 7921 (2014).
[9] T. Wang, P. Li, D. N. Chigrin, A. J. Giles, F. J. Bezares, O. J. Glembocki, J. D. Caldwell, and T. Taubner, ACS Photonics **4**, 1753 (2017).
[10] C. Wu, B. N. III, J. John, A. Milder, B. Zollars, S. Savoy, and G. Shvets, J. Opt. **14**, 024005 (2012).
[11] H. T. Miyazaki, T. Kasaya, M. Iwanaga, B. Choi, Y. Sugimoto, and K. Sakoda, Appl. Phys. Lett. **105**, 121107 (2014).
[12] J.-J. Greffet, R. Carminati, K. Joulain, J.-P. Mulet, S. Mainguy, and Y. Chen, Nature **416**, 61 (2002).
[13] D. G. Baranov, Y. Xiao, I. A. Nechepurenko, A. Krasnok, A. Alù, and M. A. Kats, Nat. Mater. **18**, 920 (2019).
[14] S. Y. Lin, J. Fleming, E. Chow, J. Bur, K. Choi, and A. Goldberg, Phys. Rev. B **62**, R2243 (2000).
[15] M. De Zoysa, T. Asano, K. Mochizuki, A. Oskooi, T. Inoue, and S. Noda, Nat. Photonics **6**, 535 (2012).
[16] M. Centini, A. Benedetti, M. C. Larciprete, A. Belardini, R. L. Voti, M. Bertolotti, and C. Sibilia, Phys. Rev. B **92**, 205411 (2015).
[17] M. Centini, M. C. Larciprete, R. L. Voti, M. Bertolotti, C. Sibilia, and M. Antezza, Opt. Express **28**, 19334 (2020).
[18] B. Auguié and W. L. Barnes, Phys. Rev. Lett. **101**, 143902 (2008).
[19] V. Giannini, A. I. Fernández-Domínguez, S. C. Heck, and S. A. Maier, Chem. Rev. **111**, 3888 (2011).
[20] V. G. Kravets, F. Schedin, and A. N. Grigorenko, Phys. Rev. Lett. **101**, 087403 (2008).
[21] G. Vecchi, V. Giannini, and J. G. Rivas, Phys. Rev. B. **80**, 201401 (2009).
[22] A. Vaskin, R. Kolkowski, A. F. Koenderink, and I. Staude, Nanophotonics **8**, 1151 (2019).
[23] R. Kolkowski and A. F. Koenderink, Proc. IEEE **108**, 795 (2020).
[24] N. Meinzer, W. L. Barnes, and I. R. Hooper, Nat. Photonics **8**, 889 (2014).
[25] F. J. G. De Abajo, Rev. Mod. Phys. **79**, 1267 (2007).
[26] V. G. Kravets, A. V. Kabashin, W. L. Barnes, and A. N. Grigorenko, Chem. Rev. **118**, 5912 (2018).
[27] M. Zhou, S. Yi, T. S. Luk, Q. Gan, S. Fan, and Z. Yu, Phys. Rev. B **92**, 024302 (2015).
[28] A. Ott, Z. An, A. Kittel, and S. A. Biehs, Phys. Rev. B **104**, 165407 (2021).
[29] E. Tervo, Z. Zhang, and B. Cola, Phys. Rev. Mater. **1**, 015201 (2017).
[30] A. Didari and M. P. Mengüç, Opt. Express **23**, A547 (2015).
[31] L. Novotny and B. Hecht, *Principles of Nano-Optics*, 2nd ed. (Cambridge University Press, 2012).
[32] P. Ben-Abdallah, S. A. Biehs, and K. Joulain, Phys. Rev. Lett. **107**, 114301 (2011).
[33] E. Tervo, M. Francoeur, B. Cola, and Z. Zhang, Phys. Rev. B **100**, 205422 (2019).
[34] M. Luo, J. Zhao, L. Liu, and M. Antezza, Phys. Rev. B **102**, 024203 (2020).
[35] F. Herz and S. A. Biehs, Phys. Rev. B **105**, 205422 (2022).
[36] R. M. Abraham Ekeroth, A. García-Martín, and J. C. Cuevas, Phys. Rev. B **95**, 235428 (2017).
[37] K. Joulain, P. Ben-Abdallah, P.-O. Chapuis, Y. De Wilde, A. Babuty, and C. Henkel, J. Quant. Spectrosc. Radiat. Transfer **136**, 1–15 (2014).
[38] A. D. Rakic, A. B. Djuriš, J. M. Elazar, and M. L. Majewski, Appl. Opt. **37**, 5271 (1998).
[39] P. Lunnemann, I. Sersic, and A. F. Koenderink, Phys. Rev. B **88**, 245109 (2013).
[40] C. M. Linton, SIAM Rev. **52**, 630 (2010).
[41] F. Capolino, D. R. Wilton, and W. A. Johnson, J. Comput. Phys. **223**, 250 (2007).
[42] S. Oroskar, D. R. Jackson, and D. R. Wilton, J. Comput. Phys. **219**, 899 (2006).
[43] S.-A. Biehs, R. Messina, P. S. Venkataram, A. W. Rodriguez, J. C. Cuevas, and P. Ben-Abdallah, Rev. Mod. Phys. **93**, 25009 (2021).

[44] G. S. Agarwal, Phys. Rev. A **11**, 230 (1975).
[45] A. E. Moskalensky and M. A. Yurkin, Rev. Phys. **6**, 100047 (2021).
[46] F. Herz and S. A. Biehs, J. Quant. Spectrosc. Radiat. Transfer **266**, 107572 (2021).
[47] C. Cherqui, M. R. Bourgeois, D. Wang, and G. C. Schatz, Acc. Chem. Res. **52**, 2548 (2019).
[48] Y. Chu, E. Schonbrun, T. Yang, and K. B. Crozier, Appl. Phys. Lett. **93**, 181108 (2008).
[49] L. Zundel and A. Manjavacas, J. Phys. Photonics **1**, 015004 (2019).
[50] S. Rodriguez, M. Schaafsma, A. Berrier, and J. Gómez Rivas, Physica B **407**, 4081 (2012).
[51] D. Wang, M. R. Bourgeois, J. Guan, A. K. Fumani, G. C. Schatz, and T. W. Odom, ACS Photonics **7**, 630 (2020).